Accurate Retrieval of Effective Magnetic Permeability in WPT Systems Using Circuit Modeling of Resonant Metasurfaces

Felipe M. Freitas, Arnaud Bréard, Loris Pace, Sandro Trindade Mordente Gonçalves, I. V. Soares, U. Resende, Christian Vollaire

Accurate Retrieval of Effective Magnetic Permeability in WPT Systems Using Circuit Modeling of Resonant Metasurfaces

F. M. Freitas[1,2], *Student Member, IEEE*, A. Bréard[1], L. Pace[1], S. T. M. Gonçalves[2], *Member, IEEE*, I. V. Soares[3], *Member, IEEE*, U. C. Resende [2], *Member, IEEE*, and C. Vollaire[1], *Senior Member, IEEE*

[1]Ecole Centrale Lyon, INSA Lyon, Université Claude Bernard Lyon 1, Ampère CNRS UMR 5005, 69134 Ecully, France
[2]Federal Center for Technological Education of Minas Gerais, DEE - PPGEL, 30421-169 Belo Horizonte, Brazil
[3]Institut d'Electronique et des Technologies du Numérique, IETR CNRS UMR 6164, 35700 Rennes, France

This paper presents a fast and accurate method for extracting the effective magnetic permeability in wireless power transfer (WPT) systems operating with resonant metamaterials. The approach combines a circuit model (CM) to compute current distribution and the Biot–Savart law to evaluate the magnetic field in 3-D space, enabling permeability retrieval without relying on complex unit-cell characterization. Two setups are validated: one with a single metamaterial (MMT) cell and another with a magnetic metasurface (MMTS) inserted between transmitter (Tx) and receiver (Rx) coils. Measurements and simulations at ISM frequencies 27.12 and 40.68 MHz show strong consistency in both magnetic response and power transfer efficiency (PTE). The proposed method captures resonant behavior and spatial variation of the magnetic field while maintaining low computational cost. Compared to full-wave simulations, the CM achieves a speedup of over 1000×, enabling the rapid evaluation of spatial configurations and permeability profiles. This capability supports efficient system design and opens paths toward metasurface optimization in near-field WPT applications.

***Index Terms*—Circuit model, effective magnetic permeability, LC metamaterial, near field, resonance, wireless power transfer.**

I. Introduction

THE effective permeability (μ_{eff}) of a two-coil system defines the interaction between the transmitting coil's (Tx) magnetic field and its surroundings, including the receiving coil (Rx). In wireless power transfer (WPT) systems based on resonant coupling, this parameter is especially relevant, as it directly impacts the strength and efficiency of near-field interactions [1], [2]. When resonant metamaterials (MMT) are introduced, effective permeability becomes crucial for enhancing coupling, concentrating fields, reducing scattering losses, and improving energy transfer efficiency, as well as for frequency tuning and minimizing loss effects to ensure optimal performance [3]–[5].

The present paper proposes a computationally fast semi-analytical method for calculating the μ_{eff} in resonant WPT systems operating at frequencies in the tens of MHz range. The approach combines circuit parameter computation with magnetic field analysis to model the system as a magnetically coupled circuit, enabling accurate current distribution through a full 3-D spatial approach. Unlike prior formulations for parameter extraction in resonant systems with magnetic metasurfaces (MMTS) or efficiency analysis in symmetrical WPT setups, the proposed approach model enables faster computation, practical system optimization, and improved accuracy [1], [6]. Furthermore, in contrast to many existing methods that rely on the complex permeability of the unit cell (the fundamental periodic element that determines the local medium's electromagnetic response in an MMTS), as presented in [6] and [2]. The proposed method provides an efficient framework for modeling and extracting the medium's μ_{eff}. This allows for a more direct assessment of system efficiency and operational characteristics. The experimental validation is presented in two scenarios: a system with two printed coils, Tx and Rx, featuring a single metamaterial cell inserted between them, and a more complex system comprising the same Tx and Rx coils but with the magnetic link between them interfaced by a full metasurface (5×5 array of MMT cell). Both cases are designed to operate near the ISM (Industrial, Scientific, and Medical) frequency bands of 27.12 and 40.68 MHz, respectively.

II. Numerical Formulation

A. Effective permeability retrieval

Magnetically coupled WPT systems enable energy transmission without the need for physical connectors by relying on magnetic coupling between coils. In a typical setup, as shown in Fig. 1(a), when the Tx and Rx coils are placed in close proximity, they generate a magnetic field oscillating at a frequency f. In this configuration, the spatial arrangement of the coils often allows for the assumption of a homogeneous magnetic flux between them. The magnetic link in such systems is governed by Ampère's law (1), which relates magnetic field circulation to current flow in the Tx coil.

$$H_{Tx1}(f) \cdot l = n \cdot I_{Tx1}(f), \tag{1}$$

where n is the number of turns in the Tx coil, l is the length of a closed contour that follows the path of the magnetic field $H_{Tx1}(f)$ through the Tx coil, and $I_{Tx1}(f)$ denotes the current flowing through the Tx coil at frequency f. The magnetic flux density $B_{Tx1}(f)$ is related to the magnetic field $H_{Tx1}(f)$ by the constitutive relation: $B_{Tx1}(f) = H_{Tx1}(f) \cdot \mu_0 \cdot \mu_r$.

Assuming in (1) $H_{Tx1}(f)$ is homogeneous along the path l, we define in (2) a frequency-dependent constant $c_{Tx1}(f)$ as the ratio between the magnetic flux density and the current in the Tx coil:

$$\frac{B_{Tx1}(f)}{I_{Tx1}(f)} = \frac{n}{l} \cdot \mu_0 \cdot \mu_r = c_{Tx1}(f). \tag{2}$$

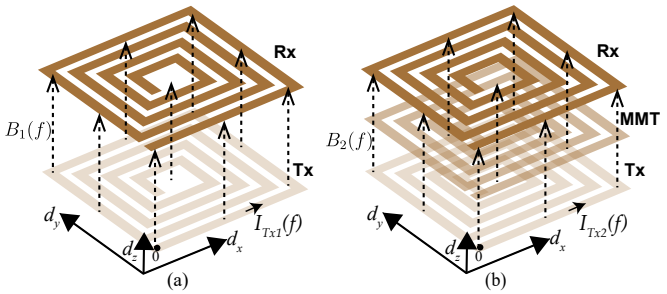

Fig. 1. Schematic of the $\mu_{\text{eff}}(f)$ extraction in WPT systems: (a) reference case with Tx, Rx coils, and without MMT, yielding field $B_1(f)$. (b) Case with MMT, resulting in modified field $B_2(f)$.

In the proposed modeling framework, two scenarios are considered: one with only the Tx and Rx coils, as shown in Fig. 1(a), and another with an additional MMT placed between them, shown in Fig. 1(b). The magnetic field $B_1(f)$ in the first case (3) includes contributions from both the transmitter ($B_{\text{Tx}}(f)$) and the receiver ($B_{\text{Rx}}(f)$) coils. When the MMT is introduced, the resulting magnetic field $B_2(f)$ includes, in addition, the field generated by induced currents circulating within the MMT ($B_{\text{MMT}}(f)$), presented in (4).

$$B_1(f) = B_{\text{Tx1}}(f) + B_{\text{Rx1}}(f) \tag{3}$$

$$B_2(f) = B_{\text{Tx2}}(f) + B_{\text{Rx2}}(f) + B_{\text{MMT}}(f) \tag{4}$$

Although the magnetic flux density varies across the metamaterial plane, values of $B(f)$ are taken to represent the local average field within a unit cell. This implies a locally homogeneous approximation, which is acceptable given that each sample corresponds to the center of a cell. The global field non-uniformity is thus discretized as a set of uniform field values, one per cell.

The effective permeability $\mu_{\text{eff}}(f)$ is then defined in (5) as the ratio between the total magnetic flux density with (4) and without the MMT (3):

$$\mu_{\text{eff}}(f) = \frac{B_2(f)}{B_1(f)}. \tag{5}$$

It is important to note that in the simulation, both configurations are driven by the same constant-voltage source. As a result, the transmitter current varies according to the total system impedance, but the voltage remains fixed. Because the magnetic field is proportional to the resulting current in each case, and this current already reflects the system's response, the ratio (5) inherently captures the relative change in magnetic behavior. Therefore, it is not necessary to explicitly divide by the current, as its effect is embedded in the field values themselves. This makes (5) a valid and practical definition for extracting $\mu_{\text{eff}}(f)$ in simulation-based analysis.

B. Circuit-based modeling of the WPT system

The WPT system, both with and without the presence of the MMT, is modeled using a circuit model (CM) approach adapted from [7]. This method enables fast and accurate computation of current distributions by solving the linear system $Z \cdot I = V$, where I is the vector of unknown currents, V is the excitation vector, and Z is the impedance matrix that includes both self and mutual impedances of all elements in the system. Fig. 2(a) presents the equivalent circuit of the complete WPT system, where the Tx and Rx coils are modeled as series RL branches, and each MMT unit cell is represented as an RLC resonator. The parasitic capacitance C_d and resistance r_d, introduced to account for dielectric influences from the substrate and surrounding medium, are included in the CM. The physical layout of the planar coil and the equivalent model of the semi-precision coaxial RF connector, type SMA (SubMiniature version A), included in CM and used in experimental validation, are shown in Fig. 2(b) and (c), respectively.

The self-inductance L of square planar coils is estimated using a semi-empirical expression [8]:

$$L = \frac{\mu_0 n^2 d_{\text{avg}} c_1}{2} \left(\ln\left(\frac{c_2}{\varphi}\right) + c_3\varphi + c_4\varphi^2 \right), \tag{6}$$

where $d_{\text{avg}} = 0.5(d_{\text{out}} + d_{\text{in}})$ is the average coil side length, d_{out}, d_{in}, are outer and inner diameter of the coil, respectively, and $\varphi = (n \cdot s)/(d_{\text{out}} - d_{\text{in}})$ is the fill factor, where s is track spacing, as shown in Fig. 2(b). For square spirals, the constants are: $c_1 = 1.00$, $c_2 = 2.46$, $c_3 = 0$, and $c_4 = 0.20$ [8].

The characteristic resistance of the coil as the sum of the ohmic resistance and a high-frequency loss component, expressed as [7]:

$$r = \frac{\rho_r \, l_{\text{coil}}}{A} + 320 \cdot \frac{\pi^4 \, d_{\text{out}}^4}{\lambda^4}, \tag{7}$$

where ρ_r is the material resistivity, l_{coil} is the total conductor length, A is the cross-sectional area ($A = w \cdot t_{cu}$) defined by width w and thickness t_{cu}, d_{out} is the outer diameter of the loop, where $\lambda = v/f$ is the signal wavelength (ratio between the speed of light v and the signal frequency f). The second term accounts for radiation and frequency-dependent losses, which become significant at high frequencies.

The parasitic capacitance C_d of each unit coil is influenced by both air and substrate permittivity, defined by:

$$C_d = (0.9\varepsilon_{\text{r,air}} + 0.1\varepsilon_{\text{r,FR-4}})\, \varepsilon_0 \frac{t_{cu}}{s} l_g, \tag{8}$$

where ε_0, $\varepsilon_{\text{r,air}}$, $\varepsilon_{\text{r,FR-4}}$, are respectively vacuum permittivity, relative permittivity of air and relative permittivity of FR-4, and l_g is the effective gap length given by: $l_g = 4 \cdot [(d_{\text{out}} - w \cdot n)(n-1) - s \cdot n(n+1)]$ [9].

The dielectric ohmic losses are captured by the resistance r_d, which is approximated as:

$$r_d = \frac{1}{\sigma} \cdot \frac{s}{4h\,(d_{\text{out}} - (2w + s))} \cdot \left(\frac{l_{\text{coil}}}{4d_{\text{out}}}\right), \tag{9}$$

where σ is the conductivity of the conductor, and h is the FR-4 thickness [9].

The SMA connector is represented by a coaxial transmission line section, modeled by its inductance (10) and capacitance (11) [10]:

$$L_{\text{SMA}} = \frac{\mu_0}{2\pi} \ln\left(\frac{b}{a}\right) \cdot l_{\text{SMA}}, \tag{10}$$

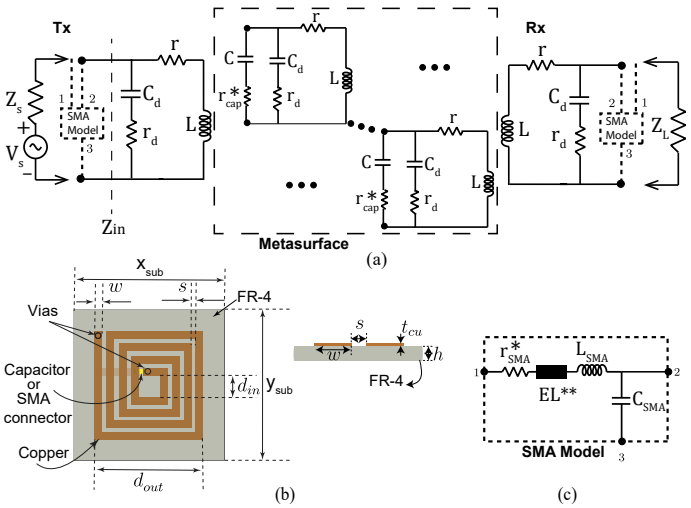

Fig. 2. The equivalent CM is used for simulating the WPT system. (a) Schematic of the CM, where Tx and Rx coils are modeled as RL branches, and MMT unit cells as RLC resonators. (b) Geometry of a square coil on an FR-4 substrate, showing key dimensions. (c) Electrical model of the SMA connector as a coaxial section with distributed elements; the parasitic inductance EL** is neglected due to its negligible effect at the frequencies considered in this work (25-45 MHz). The series resistance r^*_{SMA} and r^*_{cap} are obtained experimentally.

$$C_{\text{SMA}} = \frac{2\pi\varepsilon_r\varepsilon_0}{\ln\left(\frac{b}{a}\right)} \cdot l_{\text{SMA}}, \tag{11}$$

where a and b are the inner and outer radii of the coaxial structure, respectively, l_{SMA} is the physical length, and ε_r is the relative permittivity of the insulator. In this work, a connector with $a = 0.9\,\text{mm}$, $b = 3.2\,\text{mm}$, $l_{\text{SMA}} = 9.5\,\text{mm}$, and $\varepsilon_r = 2.1$ (Teflon) was used.

Finally, the mutual inductance M between adjacent coils or unit cells is calculated using Neumann's formula:

$$M = \frac{\mu_0}{4\pi} \oint_{\Gamma_1} \oint_{\Gamma_2} \frac{\mathrm{d}\vec{r_i} \cdot \mathrm{d}\vec{r_j}}{r_{ij}}. \tag{12}$$

The integrals in (12) are evaluated over the closed contours Γ_1 and Γ_2, which follow the current paths in loops 1 and 2, respectively. Additionally, r_{ij} denotes the distance between the differential elements dr_i and dr_j, as illustrated in Fig. 3. The same approximations employed in [7] are adopted for this calculation.

C. Magnetic flux density calculation

The magnetic flux density $\vec{B}$ in this work was computed using the Biot–Savart law, as expressed in (13). The $\vec{B}_{\text{Tx}}(f)$ corresponds to the contribution from the current flowing through the Tx coil, and it is obtained as the superposition of the magnetic flux density generated by each coil turn. It is assumed that the current in each turn is uniformly distributed and that the resulting field is spatially symmetric within the central region of interest. Fig. 3 illustrates the simulation setup, where the asterisk (*) indicates the reference point used for the magnetic flux density evaluation. Each turn of the Tx coil is modeled as a square loop composed of four straight conductive segments. The Biot–Savart integral is evaluated along these linear paths, and the $\vec{B}$ is computed at predefined observation points, specifically, at the centers of the metamaterial cells, positioned at an axial elevation in the z-direction relative to the coil that generates the field.

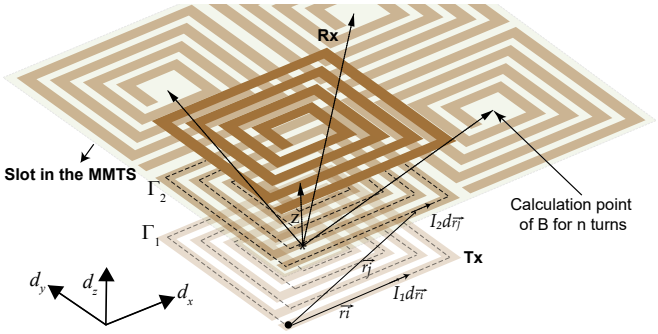

Fig. 3. Calculation of magnetic flux density B origin (*) and mutual inductance origin (•) in a WPT system with an MMTS.

$$\vec{B}(f) = \frac{\mu}{4\pi} \int \frac{I_1(f)\, d\vec{r_i} \times \hat{r}}{r^2} \tag{13}$$

In the numerical implementation, the magnetic field is first computed for a unit current (*i.e.*, $I = 1$ A), yielding a field contribution $\vec{B}_{\text{unit}}$. To reflect realistic excitation conditions, the field is then scaled by the complex excitation current $I(f)$, which may vary in magnitude and phase with frequency: $\vec{B}(f) = I(f) \cdot \vec{B}_{\text{unit}}$.

This formulation ensures that the calculated field accurately captures both the spatial geometry of the coil and the frequency-dependent nature of the excitation. The result is treated as a homogeneous average field within the transverse cross-section of each metamaterial cell. The contribution of the receiver coil, $\vec{B}_{\text{Rx}}(f)$, is computed analogously to that of the transmitter, by integrating the Biot–Savart law from the Rx center to the observation point located at the center of each MMT cell along the z-axis.

For magnetic metasurface configurations composed of multiple unit cells arranged in a periodic $n \times m$ grid, the magnetic field $\vec{B}_{\text{MMTS}}(f)$ is evaluated at each observation point, typically located at the center of each metamaterial cell at a fixed height z. The total magnetic field at a given observation point i is obtained by summing the contributions from all active sources, including the Tx coil, the Rx coil, and all metasurface cells. The general formulation is given by (14).

$$\vec{B}^{(i)}_{\text{total}}(f) = \vec{B}^{(i)}_{\text{Tx}}(f) + \sum_{j=1}^{N} \vec{B}^{(i)}_{\text{cel},j}(f) + \vec{B}^{(i)}_{\text{Rx}}(f), \tag{14}$$

where $N = n \times m$ is the total number of metasurface unit cells, $\vec{B}^{(i)}_{\text{Tx}}(f)$ is the magnetic flux density generated by the Tx coil at point i, $\vec{B}^{(i)}_{\text{cel},j}(f)$ is the contribution from cell j at point i, $\vec{B}^{(i)}_{\text{Rx}}(f)$ is the magnetic flux density generated by the Rx coil at point i.

This formulation ensures that the magnetic field calculation accurately reflects both the spatial configuration of the system and its frequency-dependent excitation characteristics, enabling a spatially resolved analysis of the complete magnetic response. Equation (14) is employed to compute B_1, corresponding to the configuration without the metamaterial, and

B_2, which represents the configuration including the MMTS structure. From these results, the effective permeability is extracted as defined in (5). It is essential to note that, in both cases, the observation point must remain the same to ensure a consistent comparison.

III. Experimental Validation of the Effective Permeability

In this work, two coil configurations were considered, based on the topology presented in [7]. Their respective characteristics are summarized in Table I, where y_{sub} and x_{sub} represent the dimensions of the FR-4 substrate on which the coils are printed. The remaining physical dimensions of the coil layout are specified in Fig. 2(b). As shown in [7], [8], the formulations employed ensure a tolerance margin of up to 3% for the characteristic parameters of the coil. Therefore, incorporating the influence of the dielectric material and the SMA connector into the model provides more accurate simulation results within the 25–45 MHz frequency range, which includes the ISM bands centered at 27.12 MHz ($\lambda \approx 11.06$ m) and 40.68 MHz ($\lambda \approx 7.38$ m).

TABLE I
Physical dimensions for the loops used in Coil 1 and Coil 2 configurations.

Coil	n	y_{sub} (mm)	x_{sub} (mm)	d_{out} (mm)	d_{in} (mm)	w (mm)
Coil 1	4	88	88	62	16	4.00
Coil 2	3	40	40	30	10	2.59

The experimental characterization of the magnetic response was performed, as shown in Fig. 4, using a Rohde & Schwarz ZVR vector network analyzer (VNA), configured in spectrum mode to operate as a signal source and receiver. The VNA generated the excitation signal and directly applied it to the transmitter coil terminals. The resulting current flowing through the coil was measured using a Tektronix P6022 current probe, which provides a calibrated voltage output proportional to the instantaneous current in the conductor. Simultaneously, the magnetic field generated by the system was captured using a Beehive Electronics 100B magnetic field probe, which features an electrostatically shielded small loop with a known transfer function. Both probes were terminated with 50 Ω loads and properly calibrated for magnitude and phase response. To ensure consistent excitation across frequency, the current signals were compensated to emulate a constant voltage source condition by applying a reference correction factor derived from a matched 50 Ω load response. This correction enables the extraction of μ_{eff} via a normalized B/I ratio, which is aligned with the theoretical condition assumed in the proposed numerical models.

A. Systems with an MMT cell

The CM method, implemented in MATLAB®, was employed to compute the currents in the Tx coil, the MMT cell, and the Rx coil, as well as the $\vec{B}$. From these quantities, the μ_{eff} was calculated using (14) at observation planes located at $z = 15\,\text{mm}$ and $z = 45\,\text{mm}$. The experimental setup consists of a Tx coil connected to an SMA source, an MMT cell loaded with a 22 pF lumped capacitor with 1% tolerance to ensure precision, placed 30 mm from the Tx coil, and an Rx coil terminated with a 50 Ω load located 60 mm from the Tx coil. Both the MMT cell and the Rx are positioned coaxially and parallel to the Tx coil, which shares the same geometry as presented in Table I for Coil 1. Current and magnetic field measurements were acquired using calibrated probes connected to a VNA, as illustrated in Fig. 4.

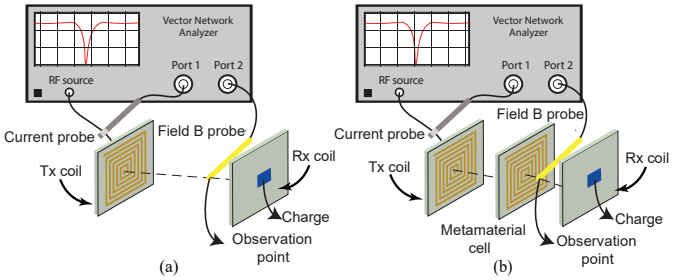

Fig. 4. Measurement setup for effective magnetic permeability retrieval in magnetic WPT systems, using the configuration (a) without MMT and (b) with MMT.

Fig. 5 presents the extracted effective permeability μ_{eff} of the WPT system with a coupled MMT cell, evaluated at axial positions $z = 15\,\text{mm}$ and $z = 45\,\text{mm}$, as shown Fig. 5(a) and (b), respectively. The plots display the real and imaginary parts of μ_{eff} obtained from measurement (black dashed), CM-based simulation (blue solid), and CST® simulation (red dash-dotted). A resonant behavior is observed near 40 MHz in both planes, with good agreement across all methods. Additionally, Fig. 5 also presents the extraction of μ_{eff} using the method described in (15), as discussed in [1]; the green dashed line represents the CST®-based result, CM-based simulation blue dashed, while the solid black line corresponds to the measurement. This formulation considers the impedance at the terminals of a loop without the metamaterial ($Z_{in}=R_{in}^{\text{loop}}+j\omega X_{in}^{\text{loop}}$) and with the metamaterial ($Z_{in}=R_{in}^{\text{loop+MMT}}+j\omega X_{in}^{\text{loop+MMT}}$).

$$\mu_{eff}=\Re(\mu_{eff})-j\Im(\mu_{eff})=\frac{X_{in}^{loop+MMT}}{X_{in}^{loop}}-j\frac{R_{in}^{loop+MMT}}{X_{in}^{loop}} \quad (15)$$

Both simulations were executed on a personal computer equipped with an Intel(R) i5-9400F processor, 16 GB of RAM, and a 2.90 GHz clock. In terms of computational efficiency, the full-wave electromagnetic simulation using CST® for the WPT system with the MMT structure required approximately 2640 seconds, excluding the postprocessing steps for effective permeability extraction. In contrast, the CM approach completed the same analysis, including postprocessing, in just 1.5 seconds, achieving a computational speedup of nearly 1760 times.

It is worth noting that the results obtained via CST® exhibit a noticeable frequency shift in both permeability extraction methods: the one proposed in this work and the approach described in [1]. However, the proposed method demonstrates improved alignment with measured data, especially when combined with the CM-based simulation, which shows consistently smaller frequency and magnitude deviations across all scenarios. As summarized in the deviation boxes in Fig. 5(a) and (b), the CM approach provides superior accuracy when compared

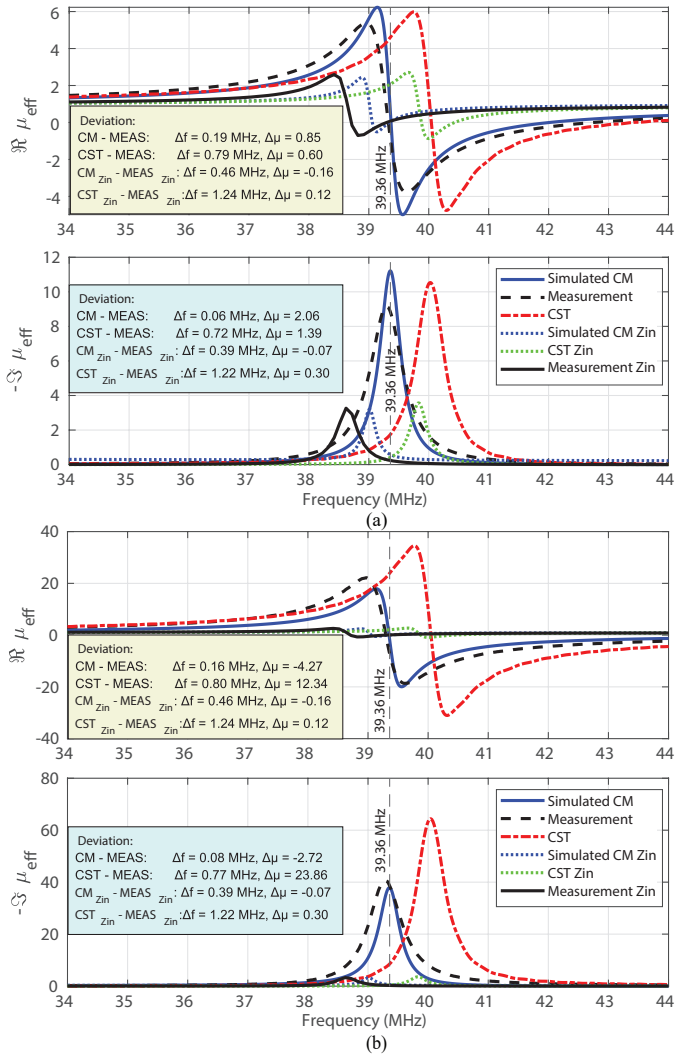

Fig. 5. Retrieval μ_{eff} as a function of frequency for observation points at (a) $z = 15\,\mathrm{mm}$ and (b) $z = 45\,\mathrm{mm}$. Real and imaginary components are shown for circuit model simulation (blue solid), measurement (black dashed), and CST® simulation (red dash-dotted). Additional extraction using the method (15) is shown for the CM (blue dashed), CST (green dotted), and measurement (black solid). The vertical line indicates the frequency at which maximum WPT efficiency occurs in the simulated CM case. Deviations for the simulated cases are presented with respect to the measured values in each scenario.

to direct CST simulations, with maximum frequency deviations reduced to below 0.5 MHz and magnitude errors typically below 1.0. This confirms the robustness of the CM-based approach. Furthermore, the method introduced in this work outperforms the traditional extraction technique by achieving better agreement with both measurement and impedance data, highlighting its reliability and practical advantages.

In Fig. 5, the resonant effect can be observed through the amplitude variation of the extracted effective permeability. This behavior can be interpreted based on the following hypothesis: at $z = 15\,\mathrm{mm}$, the μ_{eff} profile is predominantly influenced by the near-field region of the Tx coil, which is non-resonant in nature and governs the local magnetic field distribution. In contrast, at $z = 45\,\mathrm{mm}$, the resonant response of the MMT cell becomes more significant relative to the attenuated Tx field, resulting in a larger amplitude in both the real and imaginary components of μ_{eff}. This observation suggests that the enhanced response is associated with the increased contribution of the resonant field induced by the MMT structure at greater axial distances.

The performance analysis of the WPT system is conducted from two complementary perspectives: the μ_{eff} and the power transfer efficiency (PTE). The PTE of the WPT system is analyzed about the μ_{eff}, as shown in Fig. 5 and Fig. 6. The PTE is computed using the expression $\eta(\%) = |S_{21}|^2 \cdot 100\%$, based on the transmission coefficient between the transmitter and receiver. Fig. 6 shows that the system incorporating the MMT achieves a peak efficiency of 71.4% at 39.36 MHz for the simulated CM, while the measured configuration with MMT reaches 50.0% at 39.31 MHz. These frequencies of maximum efficiency closely align with the region where the real part of μ_{eff} increases and the imaginary part decreases, indicating stronger magnetic coupling and reduced reactive losses. This correlation highlights the critical role of the metamaterial-induced permeability profile in enhancing the performance of WPT systems. Despite the 21.91% difference in peak amplitude between the simulated CM-based and measured results (as shown in Fig. 6), possibly due to resistive losses in the measurement setup, the frequency of maximum efficiency shows only a small deviation of 0.05 MHz. This confirms the consistency of the resonant behavior predicted by the model.

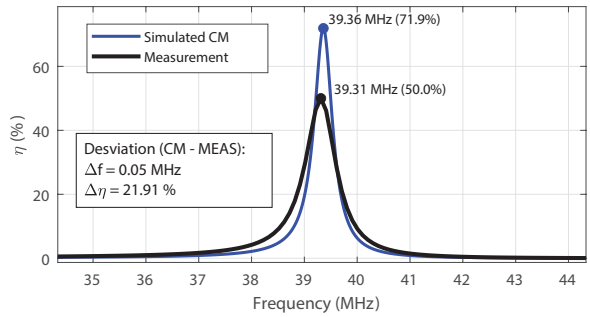

Fig. 6. Power transfer efficiency ($\eta\,(\%)$) as a function of frequency for the WPT system with MMT cell, and the CM-to-measurement deviation.

B. Systems with an MMTS

The CM method was applied to analyze a WPT system incorporating a magnetic metasurface positioned between the transmitter and receiver coils. The MMTS consists of a 5×5 array of MMT cells, each based on the geometry of Coil 2 from Table I, with a periodic spacing of 7.5 mm. Each cell is loaded with a 150 pF capacitor (1% tolerance) to establish resonance near the ISM frequency of 27 MHz. This frequency was selected to minimize resistive losses, which increase with frequency and may limit the accuracy of the model. Both the Tx and Rx coils follow the Coil 1 configuration, also defined in Table I. The MMTS is placed 3 mm above the Tx coil, while the Rx coil is located 23 mm from the Tx coil along the axial direction. The entire system is centered around cell 13, which is the central element of the MMTS grid. The observation point for μ_{eff} extraction was set at a height of 17 mm, aligned with cell 13 of the Tx coil. The setup used for computing B_1 and B_2 using (14) is illustrated in Fig. 7(a) and (b), respectively. The results obtained for this configuration are presented for both

the simulated CM case and the corresponding measurement at the defined observation point.

Fig. 7(c) presents the extracted effective magnetic permeability, both real and imaginary components, for the WPT system incorporating the MMTS. The μ_{eff} was extracted using the CM model (solid blue lines) and compared with experimental measurements (black dashed lines). A resonant behavior is clearly observed around 30.7 MHz, characterized by a peak in the real part and a corresponding dip in the imaginary component. This behavior indicates the frequency at which the MMT cells are most effectively excited, enhancing magnetic coupling. While the overall trend between simulation and measurement is consistent, a slight frequency shift and amplitude discrepancy can be seen, particularly in the imaginary part. These differences may be attributed to parasitic effects, manufacturing tolerances, or limitations in accurately modeling the physical source and material losses in the CM. Nonetheless, the result confirms that the MMTS introduces a magnetically resonant response near the intended ISM band, validating the design strategy and the suitability of the proposed extraction method.

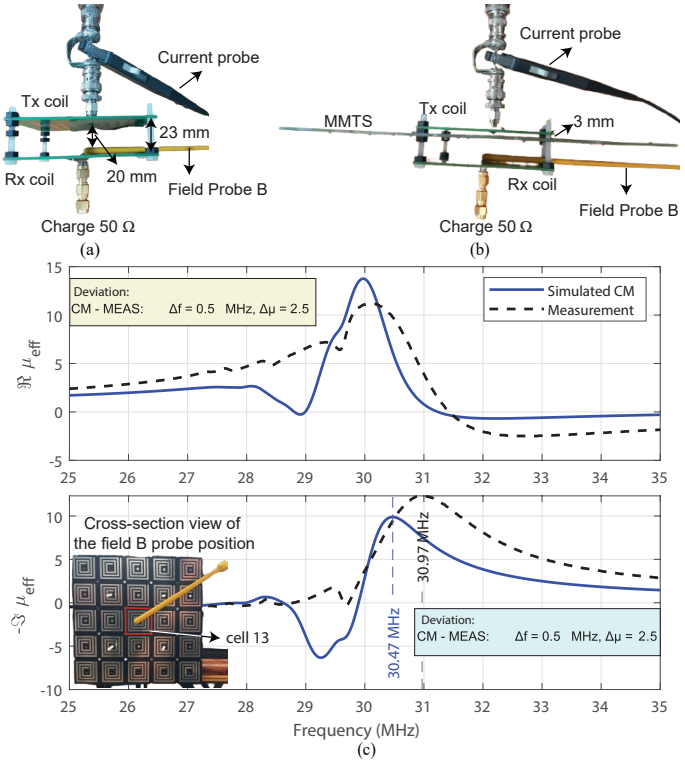

Fig. 7. Experimental setup and results for retrieval μ_{eff} extraction in the WPT system. (a) Configuration without the MMTS. (b) Configuration with the MMTS. (c) Real and imaginary components of the extracted μ_{eff} using the CM model (solid blue) and measurement (black dashed) at the observation point aligned with the central MMTS cell (cell 13). The inset shows a cross-sectional view of the probe position relative to the MMTS. The CM-to-measurement deviation is shown.

IV. Perspectives and Conclusion

This work introduced an efficient method to extract the effective magnetic permeability in resonant WPT systems with magnetic metamaterials. By combining circuit modeling and spatial field analysis, the approach was validated through two scenarios: a single MMT cell and a full MMTS.

The extracted μ_{eff} from both measurement and simulation revealed clear resonant behavior, particularly visible in the variation of its real and imaginary components near the ISM bands. The resonance observed in μ_{eff} was consistent with the frequency of maximum PTE, reinforcing the correlation between magnetic field shaping and energy transfer optimization. Although a frequency shift between measured and simulated results was observed, especially in the case of full-wave CST® simulation, this discrepancy was attributed to unmodeled source characteristics and numerical approximations. The CM-based approach, in contrast, provided results closely aligned with measurements, with frequency deviations of less than 0.5 MHz and magnitude errors of less than 1.0%. Additionally, the proposed method achieved a 1000× speedup over CST®, with only 0.05 MHz difference in peak PTE frequency, confirming its accuracy, efficiency, and practical advantages for fast permeability extraction.

Looking forward, the methodology established in this work can be extended to design and optimize non-homogeneous or spatially varying metasurfaces. The ability to evaluate the spatial magnetic response efficiently creates a foundation for implementing optimization algorithms aimed at focusing or shaping the magnetic field in specific target regions. This opens promising directions for adaptive metasurfaces, customized WPT environments, and energy delivery systems that require precise spatial control of the magnetic field.

Acknowledgment

This project was supported by CEFET-MG, CNPq, CAPES, FAPEMIG, ÉCLyon, and the École Doctorale EEA de Lyon.

References

[1] I. V. Soares, F. M. Freitas, S. T. M. Gonçalves, and Ú. C. Resende, "Integro-Differential Analysis of Resonant Magnetic Metasurfaces With Equivalent Medium Approximation," *IEEE Trans. Magn.*, vol. 59, no. 5, pp. 1–4, May 2023.

[2] W. Adepoju, I. Bhattacharya, M. Sanyaolu, and E. N. Esfahani, "Equivalent Circuit Modeling and Experimental Analysis of Low Frequency Metamaterial for Efficient Wireless Power Transfer," *IEEE Access*, vol. 10, pp. 87962–87973, 2022.

[3] X. Huang, C. Zhang, L. Cong, R. Cai, F. Yang, and C. Lu, "Development and prospects of metamaterial in wireless power transfer," *IET Power Electron.*, vol. 14, no. 15, pp. 2423–2440, Nov. 2021.

[4] W. Adepoju et al., "Critical Review of Recent Advancement in Metamaterial Design for Wireless Power Transfer," in *IEEE Access*, vol. 10, pp. 42699-42726, April 2022.

[5] I. Soares and U. Resende, "Radially periodic metasurface lenses for magnetic field collimation in resonant wireless power transfer applications," *J. Microw. Optoelectron. Electromagn. Appl.*, vol. 21, pp. 48–60, 2022.

[6] X. Huang, Z. Hou, D. Chen, R. Li, M. Shou, D. Wu, P.-a. Yang, and H. Luo, "Wireless power transfer efficiency enhancement based on a negative permeability double-helix metamaterial structure," *Int. J. Circ. Theor. Appl.*, vol. 52, no. 11, pp. 5501–5515, Nov. 2024.

[7] F. M. Freitas *et al.*, "Numerical Evaluation of Circuit Model for Fast Computational Analysis of Resonant Wireless Power Transfer System," *IEEE Trans. Magn.*, vol. 59, no. 5, pp. 1–5, May 2023.

[8] S. R. Khan, S. K. Pavuluri, G. Cummins, and M. P. Y. Desmulliez, " Wireless Power Transfer Techniques for Implantable Medical Devices: A Review ", Sensors, vol. 20, no. 12, p. 3487, Jun. 2020.

[9] X. Huang, C. Lu, and M. Liu, "Calculation and analysis of near-field magnetic spiral metamaterials for MCR-WPT application," *Applied Physics A*, vol. 126, no. 3, p. 170, 2020.

[10] T. Hirano, J. Hirokawa, and M. Ando, "Influence of the SMA connector and its modeling on electromagnetic simulation," *Microwave and Optical Technology Letters*, vol. 57, no. 9, pp. 2168–2171, Sep. 2015.